Effect of single and double tempering on corrosion behavior of modified CA6NM steel in 3.5% NaCl solution

M. Rohmah,* Moch. S. Anwar, I.N.G.P. Astawa, B. Adjiantoro, Lusiana, T.B. Romijarso and E. Mabruri

Research Center for Metallurgy, National Research and Innovation Agency (BRIN)
Gedung 460, Kawasan Puspiptek, Tangerang Selatan, 15314 Indonesia
**E-mail: miftakhur.rohmah@brin.go.id*

Abstract

The modified Ca6NM cast martensitic stainless steel (MSS) was subjected to heat treatment to explore the effect of tempering temperature and cycle on its corrosion behavior in a 3.5% NaCl solution. The metallographic observation, open circuit potential (OCP), potentiodynamic polarization and electrochemical impedance spectroscopy (EIS) were conducted to analyze the microstructure and corrosion behavior of the tempered samples. As a result of OCP and polarization test, the more positive free corrosion potential (~160 mV) and the larger passivation (~703 mV) were obtained by single tempering at 500°C (ST-500), meaning the better stability of passive layer formation. In general, the corrosion rate decreases as the temperature rises at single tempering, reaching a maximum at 550°C (0.004 mmpy), and then gradually rises in high temperature. Contrarily, double tempering tends to decrease with the temperature rising both in single and double tempering. However, double tempering has detrimental effects and barely increases the pitting resistance since the absence passivation. Conforming to the EIS analysis, the higher R_{ct} value (244 kΩ) and broader arc radius directly correlate to the oxides and hydroxides layer on the surface. The SEM observations shown that a single tempering process created the perforated pit cap at low temperatures, and the pit wasn't really visible after ST-550C.

Received: September 15, 2022. Published: November 1, 2022 doi: 10.17675/2305-6894-2022-11-4-15

Keywords: *CA6NM-2%Mo, corrosion, double tempering, polarization, single tempering, temperature tempering.*

Introduction

The effectiveness and performance of steam turbines for generating the electrical energy depends heavily on their blades. The blades are straightforwardly performed in a corrosive environment with high pressure and temperature (nearly 500°C). For achieving the optimum performance efficiently with fewest susceptibility failures at high temperatures, blades are expected to have acceptable outstanding mechanical/corrosion resistance capabilities, as strength, ductility, weldability, toughness, pitting resistance. The blades' failure is dominantly associated with fatigue, stress corrosion cracking, corrosion, and/or combination of these factors [1, 2]. A 12Cr martensitic stainless steels are commonly used for this application.

CA6NM is a cast martensitic stainless steel (MSS) with 13% Cr, 3.5–4.5% Ni, 0.4–1.0% Mo, and carbon up to 1.2% [3, 4]. Molybdenum focuses on the improving pitting and crevice corrosion resistance in a chloride environment, improving creep strength temperature, and lowering temper embrittlement [4]. However, the quench-temper process is necessary for Ca6NM steel to improve its corrosion and mechanical properties. The corrosion resistance of martensitic stainless steel is closely affected by the austenitizing temperature [5–7], certain element addition and environment control [8, 9], tempering temperature [10, 11] for delivering the passive layer on the metal surface. Several parameters influenced the hardness reduction and ductility-toughness enhancement during a single tempering process. These behaviors are caused by the differences in volume fraction, size, and type of carbide precipitation, which includes M_3C, M_7C_3, and $M_{23}C_6$ [10]. Additionally, Escobar *et al.* [12] concluded that the double-step tempering cycle heavily reduced hardness and increased the austenite reversion. As per NACE MR0175/ISO15156-2, for instance, the optimum temperature for first tempering performed between 650–690°C while the second temper was completed impressively between 593–621°C [13].

As previously stated, the double tempering process and alloy addition are needed for CA6NM steel. In the present work, electrochemical measurements in 3.5% NaCl solution are used to examine the corrosion properties of modified CA6NM at various temperatures and tempering cycle.

Materials and Method

The modified CA6NM martensitic stainless steel was manufactured by induction melting followed by casting the liquid steel in a Y block ceramic-mold. CA6NM's main composition included 2 wt.% Mo – 0.1 wt.% N, and the chemical composition for the modified steel is listed in Table 1. To explore the tempering effect, the modified CA6NM steel was treated in three stages. All samples were first austenitized for three hours at 1050°C before being oil-quenched to achieve complete martensite phase at room temperature. Then, Tempering I was conducted by heating the metal at temperatures ranging from 100 to 700°C for three hours and then quenching it in oil. The temperatures of the first tempering were 100, 200, 300, 400, 500, 550, 600, 650, and 700°C. To determine the effect of a repeated tempering process, the steel that has been tempered at 700°C was re-heated (second tempering) at 625, 650, and 675°C for three hours. ST coded samples represent single tempering, whereas DT coded samples represent double tempering.

Table 1. Chemical composition of the modified CA6NM martensitic stainless steel (wt.%).

C	Mn	Si	P	S	Cr	Ni	Mo	N	Fe
0.04	0.35	0.35	0.019	0.009	13.07	4.09	2.14	0.11	Bal.

Potentiodynamic and EIS experiment

All samples were prepared by cutting to 1×1 cm size dimension for a specimen in the polarization test. According to ASTM G61, each sample was soldered with copper wire to ensure an electrical connection. Afterward, all samples were resin-mounted and wet-ground with SiC abrasive paper (#80–1200 grit) to provide the fresh surface area. The corrosion test was conducted on a three-electrode cell system using Gamry G-750 Instruments Potentiostats. The Gamry will keep records of the increasing potential value as a function of applied current. The circuit cell system for corrosion test consists of steel sample with varying conditions as a working reference, the saturated calomel electrode (SCE) as a reference electrode, and the Platinum wire as a counter electrode, respectively. Three electrodes were held together by a caps rubber stopper and connected to the potentiostats. All tests were performed in 3.5% NaCl solution at room temperature. Before the potentiodynamic test, the specimen was immersed for 600 seconds to measure the open circuit potential (E_{ocp}). The potentiodynamic experiment was undertaken with 5 mV/s scan rate and polarization scan range of –0.5 V to 1 V.

In comparison, EIS with swept frequency ranges 0.1 Hz–100 kHz and sinusoidal AC amplitude of 10 mV/rms was used to generate an impedance spectrum. DC voltage of 8 volts and an initial delay of 200 s were applied to remove any existing oxide layer in the sample. All potentials in this paper were referred to the open circuit potential (V_{OCP}).

Result and Discussion

A. Microstructure observation

It has been known that if the CA6NM steel is quenched to room temperature from high temperature austenite state, the microstructure will consist almost completely of martensite phases with a small fraction of untransformed (retained) austenite in small fraction. The subsequence tempering of the steel transforms the martensite into typically tempered martensite, the relaxed type martensite due to carbon diffusion out of the BCT structure of the martensite. The degree of relaxation increases as the temperature and time of tempering are increased. In addition, the metallic carbides are precipitated during tempering, as the outgoing carbon reacts with carbide forming elements of Fe or Cr. The double or second tempering is usually conducted for CA6NM steel to reduce the un-tempered martensite or retained/reverse austenite. With respect to this work, the microstructure of the modified CA6NM steel after single and double tempering taken by optical microscope are shown in Figure 1. It can be seen from Figure 1(a) that the microstructure of the steel with single tempered at 550°C displays mostly tempered martensite phase. The retained austenite and carbides may exist in the microstructure in very small fraction. Other phase with an island-like shape located in some area of the microstructure is observed, *i.e.*, delta ferrite. The delta ferrite is formed during non-equilibrium solidification from high temperature or as a result of inappropriate chemical composition of the steel. At a higher tempering temperature of 700°C as shown in Figure 1(b), the martensite has experienced large strain relaxation which results in ferrite phase and larger sized carbides exist in the microstructure. In addition, the reverse austenite was characterized by white phase emerges in reasonable portion within the tempered martensite phase. Based on the literature, the existence of austenite was observed in the peak portion after tempering at 650–700°C [14]. The fresh martensite was formed from the cooling austenite when the sample being tempered at 700°C and 625°C for the first and second tempering, as presented in Figure 1(c). At a higher temperature of 675°C, second tempering results in the microstructure almost similar to that of previous first tempering at 700°C with larger size of austenite.

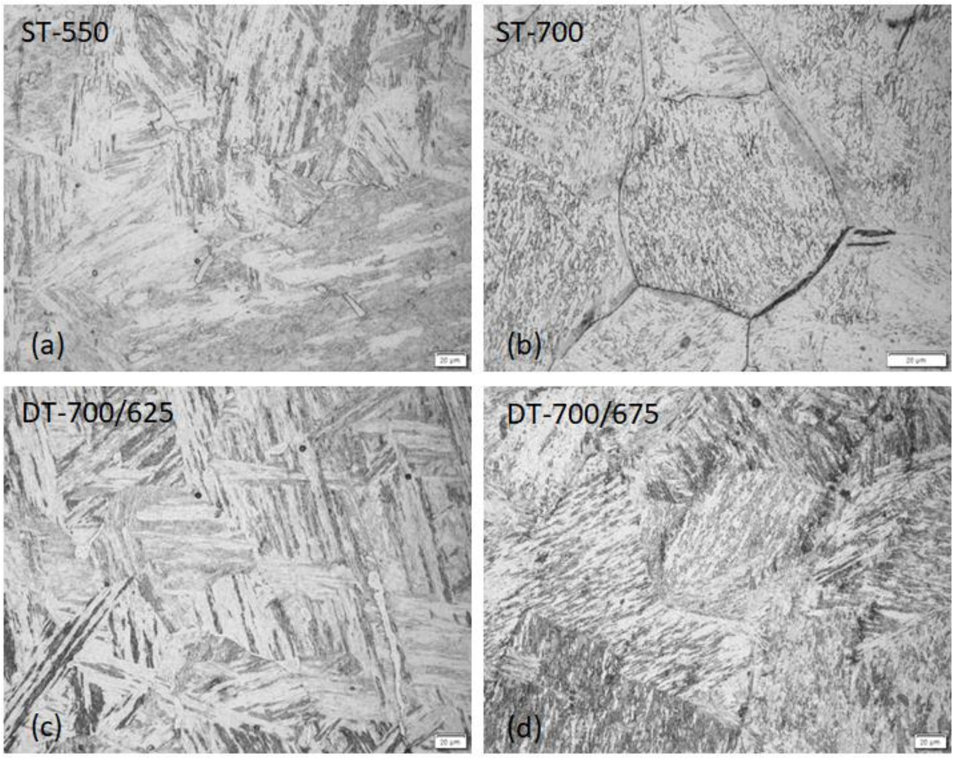

Figure 1. Microstructure of the modified CA6NM steel after single tempering at (a) 100°C, (b) 550°C, (c) 700°C, and (d) after double tempering at 675°C.

B. OCP and potentiodynamic analysis

The corrosion behavior of modified CA6NM steel was performed using OCP, potentiodynamic, and EIS tests. The open circuit potential (OCP) curve of modified CA6NM which subjected to tempering at various temperature is shown in Figure 2.

The OCP indicated that the total anodic current is equivalent to the cathodic current, concerning placed reference electrode in the electrolyte. Based on Figure 2, the shapes of all curves OCP were similar, slightly dropping towards lower values with time increased as a consequence of the interaction between metals and electrolytes. As the temperature tempering increases, the OCP curve of the single tempered steel (Figure 1a) was shifted upward to positive and reaches a maximum value at 500°C. On tempering over 500°C, the OCP was found to drop respectively. The tendency of the OCP curve was similar to the result from Rajasekhar [15]. OCP peak ST-500C has the highest OCP value in positive potential (160 mV to 18.72 mV), indicating the lower corrosion rate for further increased corrosion resistance. The more negative OCP, the greater the corrosion occurrence. The increased value of OCP for ST-500C might be attributed to the decreased volume fraction of martensite phase, increased fraction of austenite reversion, and tempering temperature increased [12, 16]. The higher the tempering temperature, the faster the reversion kinetics, resulting in a higher amount of reverted austenite before cooling. In addition, the chromium carbide, which precipitated at a maximum temperature of 500–550°C, was more electropositive than steel matrix and initiates localized corrosion [15]. Compared to ST-550C, the ST-500C steel sharply decreases the OCP value. So, a stable free corrosion was obtained by ST-550C.

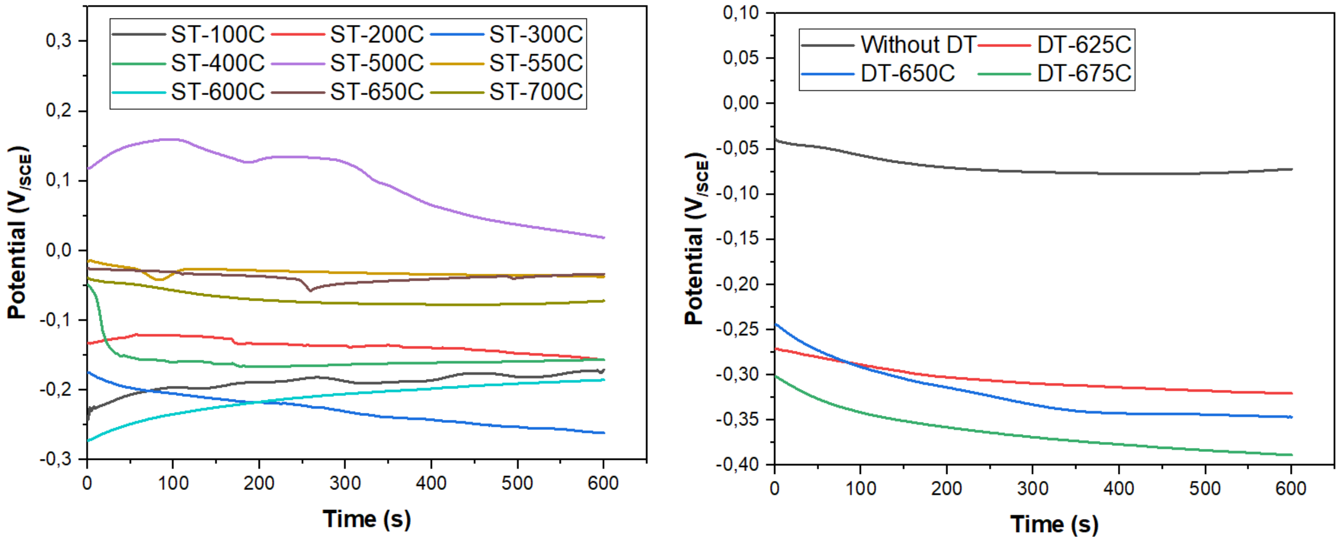

(a) **(b)**

Figure 2. OCP of modified CA6NM steel subjected to (a) Single and (b) Double Tempering.

Double tempering has negative effects on corrosion behavior, specifically decreasing an OCP value. The curve was dramatically shifted downward as the temperature of doubles tempering increased. The curve has been stable at –320.3 mV, –346.5 mV, and –388.5 mV for 625, 650, and 675°C of double tempering temperature, respectively. Previous work concluded that the results of the microstructure of the single (around at 600–700°C) and double (approximately at 620–630°C) tempering processes are light similar to those of quench tempering, namely, the structure of finely tempered martensite with the ferrite phase and retained austenite island [17]. The finer microstructure causing a larger surface area for corrosion site and lead to higher corrosion rate. Also, sensitization might occured at tempering temperatures above 450°C due to the initiation and growth of chromium carbide [18].

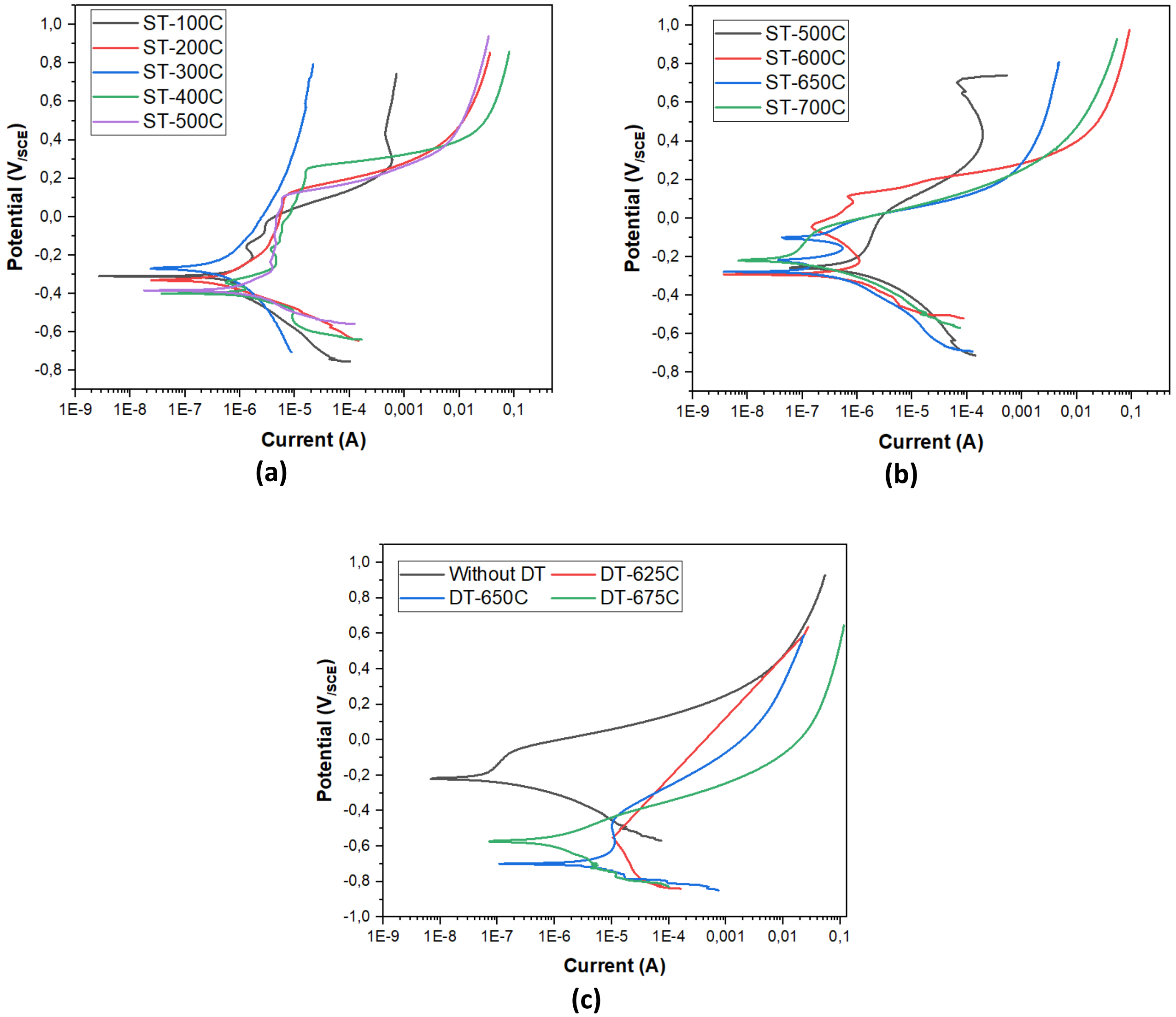

(a) (b) (c)

Figure 3. Potentiodynamic Curve of (a) Single Tempering 100–500°C, (b) Single Tempering 550–700°C, and (c) Double Tempering.

Potentiodynamic curve recorded for CA6NM with various temperature of single and double tempering in the 3.5% NaCl solution are illustrated in Figure 3, respectively. The corrosion parameters of modified CA6NM, including the corrosion potential (E_{corr}), corrosion current (I_{corr}), and corrosion rate, are summarized in Table 2 and 3. In the cathodic zone of all samples, a pseudo plateau due to oxygen reduction in a uniformly active surface is observed, indicating the most of oxides was reduced [19]. Figure 3(a, b) shows that modified CA6NM-single tempered steel has a small tendency for passive region formation, followed by pitting (transpasive mechanism). A double-tempered sample did not have a clear passive zone (Figure 3c). Based on Table 2, the passivation potential (E_{pass}) values were followed: 315 mV, –140.4 mV, 79.3 mV, –219.3 mV, –244.4 mV, 356.4 mV, –176.2 mV, –140.1 mV, and –160 mV for single tempered process. The vast passivation potential (E_{pass})

increased with the increasing temperature and reached a maximum value at 400°C of single tempered temperature, was started from –219.3 to 251.9 mV at 17.8 μA/cm^2 of current density. The ST-550C has greater and wider passivation potential in postive potential (around 703 mV) indicating the better stability of passive layer and lower corrosion rate on it's steel surface [9]. A 13% Cr provided the chromium-rich of inner passive layer on the surface metals. Besides that, the 2 wt.% Mo addition in CA6NM steel has a positive effect, likely, inhibited the pit initiation, rendered the passive layer more stable against breakdown, and facilitated the re-passivation in alkaline electrolyte [20].

Table 2. The potential and current density of passivation, pitting, and dissolution of modified CA6NM in 3.5% NaCl.

Sample	E_{pass} (mV/SCE)	I_{pass} μA/cm^2	E_{pit} (mV/SCE)	$E_{dissolution}$ (mV/SCE)
ST-100C	315	585	457.8	423.8
ST-200C	–140.4	3.43	109.3	264
ST-300C	79.3		–	–
ST-400C	–219.3	4.58	251.9	470.9
ST-500C	–244.4	3.68	104.2	353
ST-550C	356.4	164	703.8	–
ST-600C	–176.2	0.84	–31.35	368.3
ST-650C	–140.1	0.47	–92.22	121.4
ST-700C	–160	0.08	–75.19	234.4

In addition, pitting corrosion occured in the positive potential for the samples of 100–500°C single tempered, while for temperature tempering above 500°C samples, pitting occured in negative potential, inversely. The fluctuations of potentiodynamic electrochemical curve can be attributed to the solubility of an element in the matrix and related to the formation, growth, re-passivation of metastable pits as active site in terms of inclusion form [5, 21]. The decreased of E_{pit} value, from 457.8 mV (ST-100C) to –75.19 mV (ST-700C), was caused by the M_3C carbide precipitated in the matrix and the size growth as increasing the temperature temper. The M_3C carbide, which has more localized Cr content and lead to chromium depletion in the grain boundaries, acts as a preferential site for pitting formation [18, 22]. A sharp curve increased after the transpassive region, indicating the breakdown of passive layer by chloride ions attack and further leading to the higher carbide dissolution and accelerating the active corrosion [18]. The current density increased rapidly after the potential reached the pitting potential (E_{pit}), known as the trans-passivated zone. Double tempering did not improve the pitting corrosion resistance due to the absence of passivation, as shown in Figure 3(c). As the temperature increased in double tempering, the corrosion rate increased to 1.177 mmpy.

Table 3. OCP and Potentiodynamic Result of CA6NM-2%Mo in 3.5% NaCl Solution.

Materials	**Heat treatment**	***OCP* (mV/SCE)**	**Potentiodynamic**				**Ref.**
			β_a (mV/decade)	**E_{corr} (mV)**	**I_{corr} μA/cm^2**	**Corrosion rate (mmpy)**	
CA6NM-Single Tempering	ST-100C	–170.6 to –242.2	214.7	–309.3	0.622	0.284	*
	ST-200C	–120.4 to –156.7	210.1	–330.4	0.514	0.235	*
	ST-300C	–261.1 to –174.6	309.8	–270.3	0.405	0.185	*
	ST-400C	–166.1 to –49.5	50.42	–383.0	0.449	0.105	*
	ST-500C	18.7 to 160	96.49	–399.2	0.184	0.084	*
	ST-550C	–14.0 to –41.9	130.1	–253	0.068	0.004	*
	ST-600C	–271.5 to –185.4	100.4	–291.0	0.301	0.137	*
	ST-650C	–57.4 to –25.2	70.91	–220.1	0.073	0.033	*
	ST-700C	–0.077 to –0.039	61.72	–220.1	0.014	0.006	*
CA6NM-Double Tempering	DT-625C	–0.32 to –0.27	116.4	–354.2	3.567	1.63	*
	DT-650C	–0.35 to –0.24	107.0	–723.6	4.874	2.227	*
	DT-675C	–0.39 to –0.30	115.0	–851.4	2.576	1.177	*
13%Cr (MSS)	Anneal 850°C + austenitizing 980–1130°C	–0.25 to –0.175	Not reported	–250 to –200	0.002	Not reported	[5]
X46Cr13	Austenitizing 1000–1200°C	Not reported	Not reported	–740 to –680**	5–15 ×10^{-3}	Not reported	[6]
3Cr13 (MSS)	Anneal 980°C + tempering 280–600°C	Not reported	Not reported	–0.311 to –0.493	954 to 20·10^3	Not reported	[10]
13Cr3Mo	Tempering 625°C for 1 h	Not reported	244.4	Not reported	2.09	0.0087 mmpy	[23]

*The present work; ***versus* Ag/AgCl electrode.

C. EIS study

For detailed analysis of the passivation behavior of CA6NM-2%Mo in 3.5% NaCl solution, EIS measurements were performed by Nyquist, Bode modulus, and Bode phase plot, shown in Figures 4, 5.

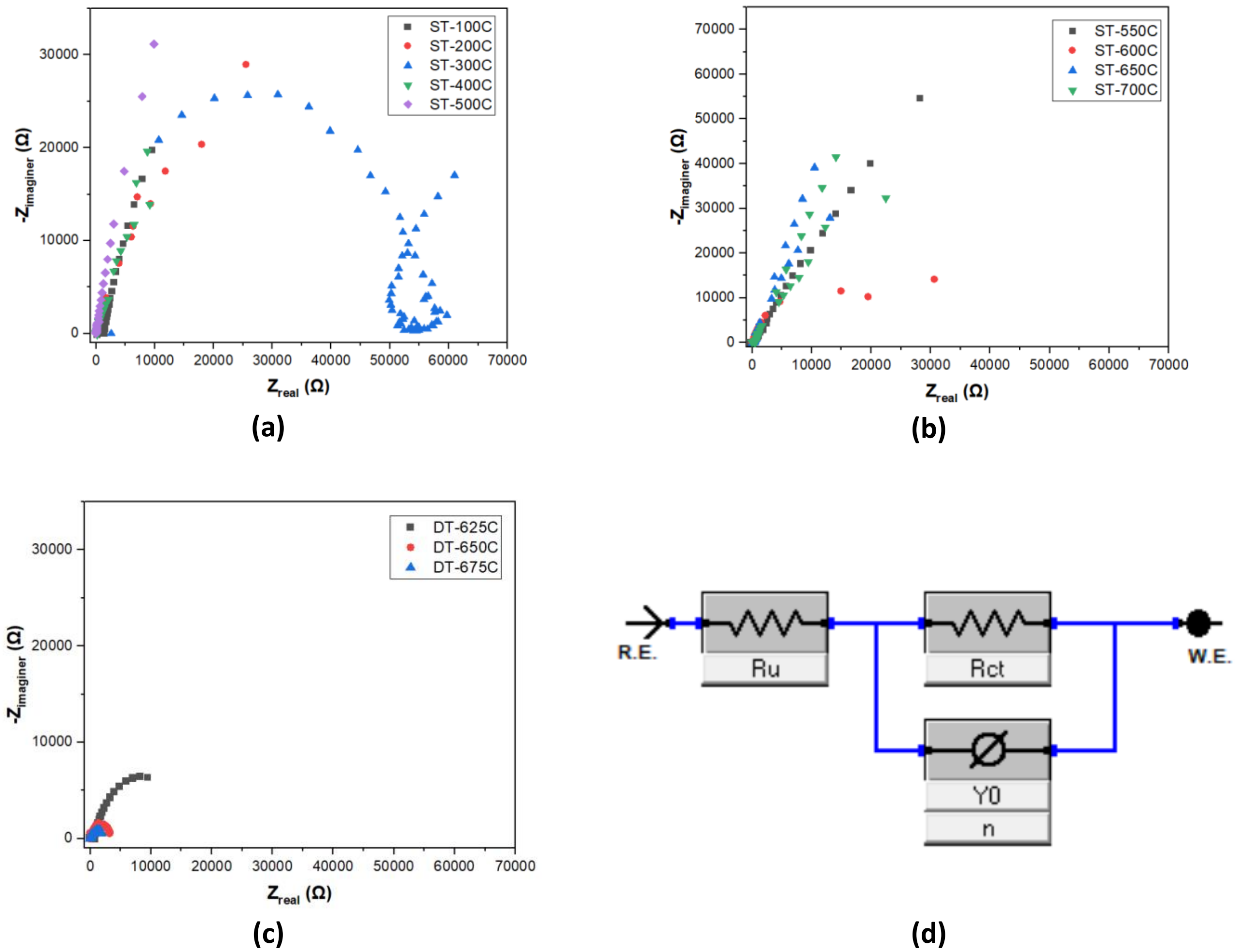

(a)

(b)

(c)

(d)

Figure 4. Nyquist plot of modified CA6NM after (a) single tempering at 100–500°C (b), single tempering at 550–700°C, (c) double tempering at 625–675°C, and (d) equivalent electrical circuit for all samples.

Nyquist plot of CA6NM-2%Mo in Figure 4 shows that the real impedance |*Z*′| versus imaginer |*Z*”| of all tempered samples exhibited an un-finished semi-circle curve with single capacitive loop at low frequency, which was associated with solution resistance (R_s) and capacitance of double layer *CPE* (Y_0), charge transfer resistance (R_{ct}) at the metal-electrolyte interface. The temperature-tempering variation affected the size and radii angle, but their value fluctuated in single tempered sample (Figure 4a,b). The larger arc diameter and higher Z_{imaginer} |*Z*″| were obtained by ST-300C sample, while ST-500C and ST-550C received the larger arc radii, indicating their condition could tend to be more significant passive film and decreasing the corrosion rate. The elevated R_{ct} value is 244 kΩ for ST-500C and 227 kΩ for ST-550C. The higher of R_{ct} value was directly linked to the oxides and hydroxides compound in the surface film formation [10]. The impedance has been fitted to determine the best equivalent electrical circuit (EEC) models and to predicted a corrosion mechanism for CA6NM-2%Mo in 3.5% NaCl solution. The best fitted electrical circuit is shown in

Figure 4d, consisting of the solution resistance (R_s) in series with a parallel-connected element (constant phase element and charge transfer resistance, $CPE///R_{ct}$). *CPE* is typically modeled for the uniform distribution current with high surface roughness due to inhomogeneity in the passive layer of stainless surface [8]. This circuit has been proposed by Lu *et al.* [5] and Lian *et al.* [10] for NaCl solution and by Nikitasari [24] for CA6NM modified in geothermal brine.

As is shown in Figure 4c, the diameter and radii angle of the impedance of DT-625℃ was significantly larger than other temperature, and the diameter decreased with the temperature, indicating that the lower temperature of double tempering (DT) could form less stability of passive layer and reducing the corrosion resistance of CA6NM-2%Mo in 3.5% NaCl.

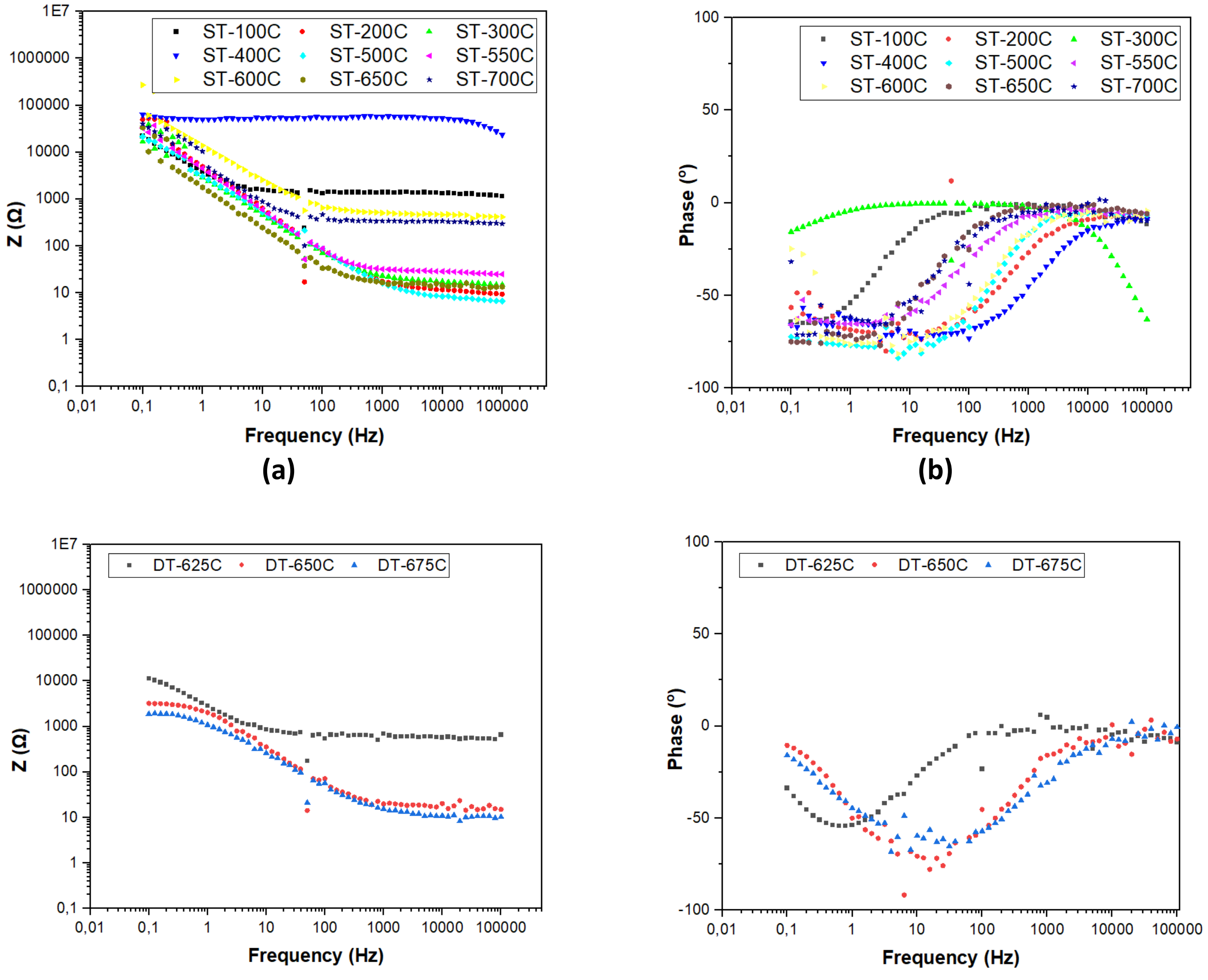

(a) (b)

(c) (d)

Figure 5. Bode (a) Modulus and (b) phase in Single Tempering; Bode (c) Modulus and (d) phase in Double-Tempering.

Figure 5 shows that the Bode Modulus (freq *vs.* *Z* curve) and Bode phase plot (Freq *vs.* phase angle curve) have similar impedance diagram for single and double tempering sample.

Bode Modulus (Figure 5a dan 5c) shows that the impedance |*Z*| of all samples drops slightly towards the lower value with a slope close to –1 at low-middle frequency parts (f<10 Hz). The impedance spectra at high frequency are most related to protective passive layer response or not [25]. ST-400C has a different pole in module impedance; it's more stable for low-high frequency, indicating the higher self-passivation. The high modulus impedance under low frequency ranges from 10^4 Ω to 10^5 Ω, typically passive film and related to the interface polarization resistance [25]. In addition, the phase angle increased near zero degrees at low frequency (f<10 Hz), indicating the capacitive behavior is dominated in mechanism, and the CA6NM-2%Mo surface is resistant to aggressive species (Cl^-), further leading to the protective of oxide layer formation [24].

Table 4. The fitting result of Impedance spectra for CA6NM-2%Mo in 3.5% NaCl solution.

Material		R_p (kΩ)	R_s (Ω)	Y_0 ($s^n\Omega^{-1}$)	N
Single Tempering	ST-100C	62.3	853	6.19×10^{-5}	0.8773
	ST-200C	23.1	11.89	2.79×10^{-5}	1
	ST-300C	54.1	1.077	8.79×10^{-11}	0.9738
	ST-400C	86.9	7.222	6.78×10^{-5}	0.8092
	ST-500C	244	27.8	4.08×10^{-5}	0.9389
	ST-550C	227	447.4	1.56×10^{-5}	0.833
	ST-600C	20.1	14.56	9.80×10^{-5}	0.9356
	ST-650C	85.6	272.8	2.83×10^{-5}	1
	ST-700C	61.8	219.1	1.71×10^{-5}	1
Double Tempering	DT-625C	14.8	425	7.54×10^{-5}	0.85
	DT-650C	2.52	16.98	3.92×10^{-5}	1
	DT-675C	1.97	11.07	1.37×10^{-4}	0.92

The value of n indicates the nature of *CPE*, namely $n=1$ for an ideal capacity, $n=0$ for resistance, and $n=-1$ for pure inductance. The n value varies in the ranges of 0.833–1, indicating the *CPE* is in good agreement with capacitive behavior. A smaller Y_0 value can be associated with the thicker or more homogeneous passive layer [6, 23]. But some researchers have concluded that the effective capacitance (C_{eff}) is proportional to Y_0^{-n}. As mentioned in Table 4, the smaller of Y_0 values were obtained at ST-300C and ST-550C, approximately $8.79\times10^{-11}\ s^n\,\Omega^{-1}$ and $1.56\times10^{-5}\ s^n\,\Omega^{-1}$. However, ST-300 has no pitting tendency at high potential (Figure 3a) and a moderate corrosion rate (0.185 mmpy). So, the ST-550C has better corrosion resistance. A thickening of the passive film of Cr oxides is contributed by the presence of Mo^{4+} and Mo^{6+} [20].

D. SEM analysis

The effect of tempering temperature on the pit growth behavior of the modified Ca6NM surface was observed by scanning electron microscope (SEM) and depicted in Figure 6. The circular of closed pit was obtained by ST-400C and ST-500C (Figure 6a–c). The perforated pit cap indicated the passivity breakdown on the oxide layer of the Ca6NM surface, and the cathodic reaction with lower current density (β_a) occurs near the pit mouth, which reduces the corrosion rate to ~0.084 mmpy. The passive film involved the precipitated thin salt (Figure 6b) from a porous outer layer [26]. On the contrary, as shown in Figure 5d, the pit was clearly invisible, indicating the tempering process at 550°C given better pitting resistance due to the high positive of the potential pit (E_{pit}~703.8 mV). As the temperature was above 550°C, the E_{pit} shifted towards the negative direction (Table 2), the pit size increased, and the perforated caps were removed to give an open hemispherical pit [26]. The imperfect-open pit was obtained by ST-600C and ST-700C (Figure 6e–f). Combining of Cl^- and Fe^{2+} hydrolysis can accelerate the dissolution of the passive film and result in a pitting attack [27].

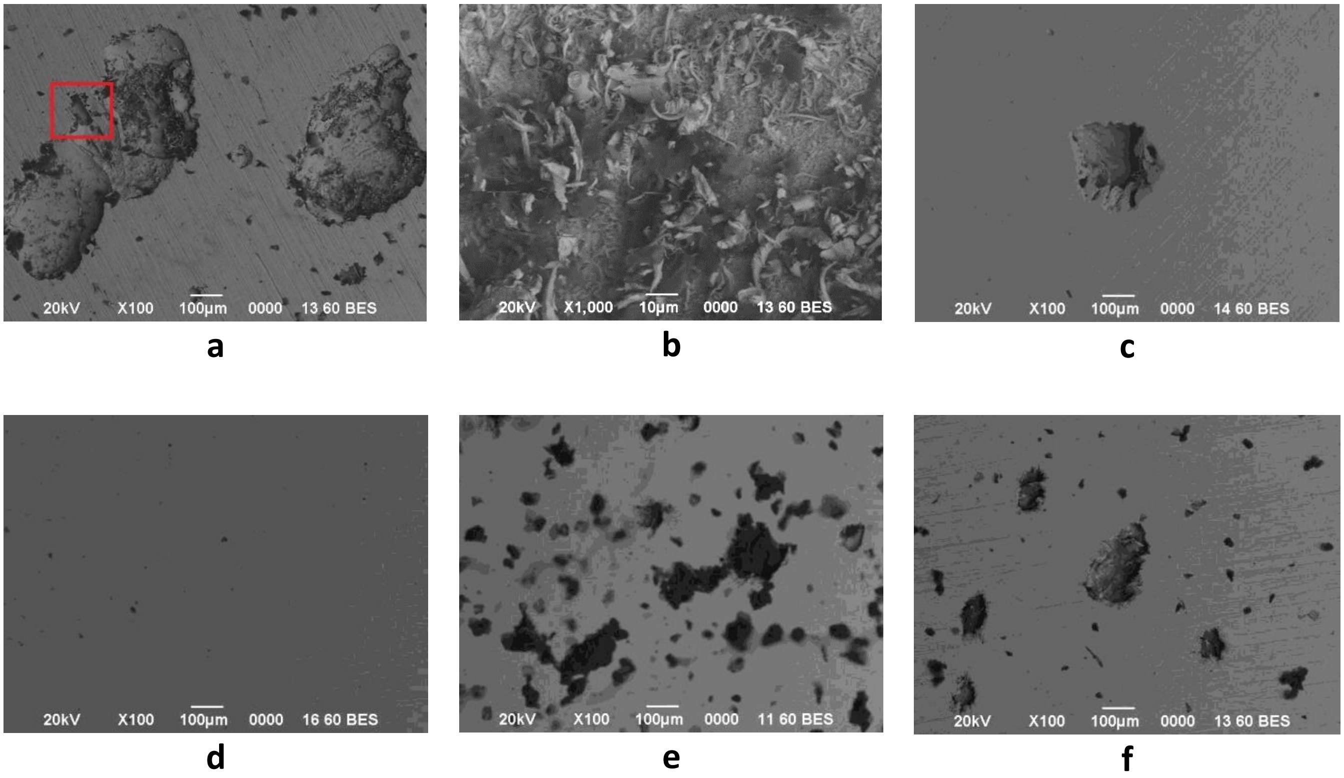

Figure 6. Morphology of corroded samples (a) ST-400C, (b) red box area or salt precipitate (c) ST-500C, (d) ST-550C, (e) ST-600C, and (f) ST-700C after polarization test in NaCl 3.5% solution.

In addition, EDS analysis was subjected to investigate further the effect of tempering temperature on the passive film formation of Ca6NM surface. As shown in Figure 7, the Cr, Ni, and Mo level were slightly increased along with the tempering temperature increased and reached its maximum by ST-500C. Then, it decreased approximately to ~16.54%, 1.01%, and 1.45% for Cr, Ni, and Mo content, respectively. The results suggested that the tempering temperature above 500°C has significant tends a passive layer's porous and increases the dissolution rate of salt film inside the pit [22, 28].

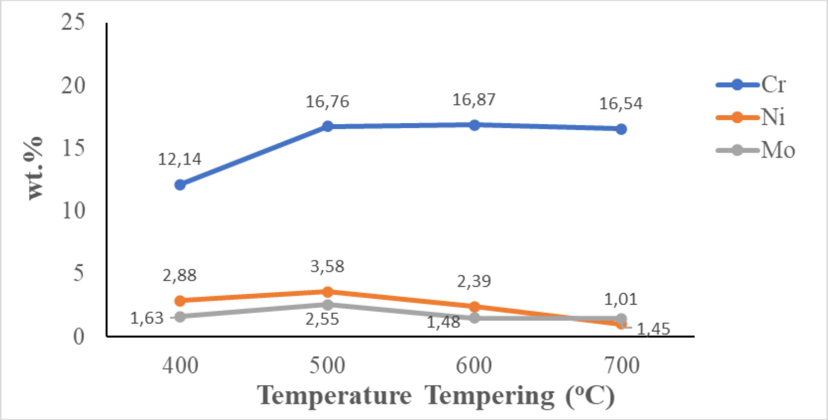

Figure 7. Effect of tempering temperature on the Cr, Ni, and Mo content of the oxide layer.

Conclusion

The single and double tempering with varying temperature influenced the microstructure, which in response had an impact on the corrosion behavior of Modified Ca6NM steel. As a tempering result, the microstructure consists of almost fully tempered martensite with modest amounts of delta ferrite, retained austenite, and carbides. As the temperature of temper increases, the martensite relaxation increases due to the faster carbon diffusion out of the BCT structure and martensite fraction decreases, which improves the corrosion resistance. In terms of corrosion behavior, the Modified Ca6NM that single tempered at 550°C exhibits most excellent corrosion resistance (0.004 mmpy) due to the self-passivation reaction in the metal surface. The E_{pit} shifted towards the negative direction, the pit size expanded, and the perforated caps were removed to reveal an open hemispherical pit as the temperature of the single temper process rise above 550°C. Furthermore, the double tempering (DT) process increases corrosion rate, notably lowering the *OCP* value. The corrosion rate increases as the temperature rises, 1.177 mmpy for DT-675 sample. The polarization curve is dramatically shifted downward as the temperature of doubles tempering increased to 675°C due to the finer microstructure outcomes. Additionally, the greater the radius and the reduced the diameter of the arc EIS further confirm the lowest stability of the passive layer and the poorer corrosion resistance.

Acknowledgment

All authors would like to express their gratitude to Research Centre for Metallurgy – National Research and Innovation Agency (BRIN) of Indonesia for providing the facilities and financial support in this research.

Reference

1. A. Rivaz, S.H.M. Anijdan and M. Moazami-Goudarzi, Failure analysis and damage causes of a steam turbine blade of 410 martensitic stainless steel after 165,000 h of working, *Eng. Failure Anal.*, 2020, **113**, 104557. doi: 10.1016/j.engfailanal.2020.104557
2. M.C.A. Harison, M. Swamy, A.H.V. Pavan and G. Jayaraman, Root Cause Analysis of Steam Turbine Blade Failure, *Trans. Indian Inst. Met.*, 2016, **69**, no. 2, 659–663. doi: 10.1007/s12666-015-0750-2
3. Y. Murakami, 17 – Martensitic stainless steels, *Metal Fatigue (Second Edition)*, Elsevier Ltd, 2019, 431–451. doi: 10.1016/b978-0-12-813876-2.00017-0
4. R. Hill and A.L. Perez, 26 – New steels and corrosion-resistant alloys, *Trends in Oil and Gas Corrosion Research and Technologies*, Elsevier Ltd., 2017, 613–626. doi: 10.1016/B978-0-08-101105-8.00026-7
5. S.Y. Lu, K.F. Yao, Y.B. Chen, M.H. Wang, Y. Shao and X.Y. Ge, Effects of austenitizing temperature on the microstructure and electrochemical behavior of a martensitic stainless steel, *J. Appl. Electrochem.*, 2015, **45**, no. 4, 375–383. doi: 10.1007/s10800-015-0796-1
6. I. Bösing, L. Cramer, M. Steinbacher, H.W. Zoch, J. Thöming and M. Baune, Influence of heat treatment on the microstructure and corrosion resistance of martensitic stainless steel, *AIP Adv.*, 2019, **9**, no. 6, 065317. doi: 10.1063/1.5094615
7. A. Yilmaz, X. Li, S. Pletincx, T. Hauffman, J. Sietsma and Y. Gonzalez-Garcia, Passive Film Properties of Martensitic Steels in Alkaline Environment: Influence of the Prior Austenite Grain Size, *Metals*, 2022, **12**, no. 2, 292. doi: 10.3390/met12020292
8. L. Quan-de, R. Dou, Z. Fu-qiang, G. Wei-hua, G. Zhen-huan, G. Xiu-fang, L. Bin, Y. Ming, N. Rong and M. Hui-min, Research on the corrosion behavior of 14Cr12Ni3Mo2VN stainless steel in a NaCl solution with different pH, *Int. J. Electrochem. Sci.*, 2020, **15**, 2166–2179. doi: 10.20964/2020.03.05
9. J. Kang, J. Li, K.Y. Zhao, X. Bai, Q.L. Yong and J. Su, Passivation Behaviors of Super Martensitic Stainless Steel in Weak Acidic and Weak Alkaline NaCl Solutions, *J. Iron Steel Res. Int.*, 2015, **22**, 1156–1163. doi: 10.1016/S1006-706X(15)30127-8
10. Y. Lian, J. Zhang, P. Ji, Z. Zhang, M. Ma, Ch. Zhao and J. Huang, Effect of Tempering Treatment on Atmospheric Corrosion Behavior of 3Cr13 Martensitic Stainless Steel in Marine Environment, *J. Mater. Eng. Perform.*, 2022, **31**, 4963–4973. doi: 10.1007/s11665-022-06597-8
11. I.A. Channa, A.A. Shah, S.H. Abro and M. Ali, Effect of Tempering Temperature on the Properties of Martensitic Stainless Steel AISI-420, *Sukkur IBA J. Emerg. Technol.*, 2019, **2**, no. 1, 51–56. doi: 10.30537/sjet.v2i1
12. J.D. Escobar, J.P. Oliveira, C.A.F. Salvador, A.P. Tschiptschin, P.R. Mei and A.J. Ramirez, Double-step inter-critical tempering of a supermartensitic stainless steel: Evolution of hardness, microstructure and elemental partitioning, *Mater. Charact.*, 2019, **158**, 109994. doi: 10.1016/j.matchar.2019.109994

13. International standard NACE MR0175/ISO15156-2, Petroleum and Natural Gas Industries – Materials for Use in H_2S Containing Environments in Oil and Gas Production – Part 2: Cracking-Resistant Carbon and LowAlloy Steel, and the Use of Cast Iron., 2003.
14. B.A. Tabatabae, F. Ashrafizadeh and A.M. Hassanli, Influence of retained austenite on the mechanical properties of low carbon martensitic stainless steel castings, *ISIJ Int*., 2011, **51**, no. 3, 471–475. doi: 10.2355/isijinternational.51.471
15. A. Rajasekhar, Corrosion Behavior of Martensitic Stainless Steels Role of Composition and Heat Treatment Procedures, *Int. J. Sci. Res*., 2015, **4**, no. 4, 2795–2798.
16. Y. Zhao, W. Liu, Y. Fan, T. Zhang, B. Dong, L. Chen and Y. Wang, Influence of microstructure on the corrosion behavior of super 13Cr martensitic stainless steel under heat treatment, *Mater. Charact*., 2021, **175**, 111066. doi: 10.1016/j.matchar.2021.111066
17. M. Ramos-Azpeitia, J.A. Ruiz-Ochoa, J.L. Hernandez-Rivera and C.A. Perez-Alonso, Heat Treatment Optimization of CA-6NM Cast Alloy Using a Full Factorial Design of Experiments Approach, *Int. J. Metalcast*., 2021, **15**, no. 1, 76–87. doi: 10.1007/s40962-020-00445-y
18. I. Taji, M.H. Moayed and M. Mirjalili, Correlation between sensitisation and pitting corrosion of AISI 403 martensitic stainless steel, *Corros. Sci*., 2015, **92**, 301–308. doi: 10.1016/j.corsci.2014.12.009
19. S. Marcelin, N. Pébère and S. Régnier, Electrochemical characterisation of a martensitic stainless steel in a neutral chloride solution, *Electrochim. Acta*, 2013, **87**, 32–40. doi: 10.1016/j.electacta.2012.09.011
20. T.J. Mesquita, E. Chauveau, M. Mantel and R.P. Nogueira, A XPS study of the Mo effect on passivation behaviors for highly controlled stainless steels in neutral and alkaline conditions, *Appl. Surf. Sci*., 2013, **270**, 90–97. doi: 10.1016/j.apsusc.2012.12.118
21. J.Y. Park and Y.S. Park, The effects of heat-treatment parameters on corrosion resistance and phase transformations of 14Cr–3Mo martensitic stainless steel, *Mater. Sci. Eng., A*, 2007, **448–451**, 1131–1134. doi: 10.1016/j.msea.2006.03.134
22. A.N. De Moura, C.M. de Alcântara, M.T. D’Azeredo Orlando, W. da Silva Labiapari, M.A. da Cunha, T.R. de Oliveira and V.T.L. Buono, Microstructure and Pitting Corrosion Resistance of Quenched, Single Tempered and Double Tempered AISI 420 Martensitic Stainless Steel, *Mater. Res*., 2021, **24**, no. 6, e20210093. doi: 10.1590/1980-5373-MR-2021-0093
23. M.S. Anwar, T.B. Romijarso and E. Mabruri, Pitting resistance of the modified 13Cr martensitic stainless steel in chloride solution, *Int. J. Electrochem. Sci*., 2018, **13**, 1515–1526. doi: 10.20964/2018.02.13
24. A. Nikitasari, E. Mabruri and R. Riastuti, Corrosion behavior of ca6nm in simulated geothermal brine highlighted by electrochemical impedance spectroscopy (Eis), *Eng. Appl. Sci. Res*., 2021, **48**, no. 4, 359–367. doi: 10.14456/easr.2021.38

25. M. Monnot, V. Roche, R. Estevez, M. Mantel and R.P. Nogueira, Molybdenum effect on the Sulfide Stress Corrosion of a super martensitic stainless steel in sour environment highlighted by Electrochemical Impedance Spectroscopy, *Electrochim. Acta*, 2017, **252**, 58–66. doi: 10.1016/j.electacta.2017.08.165
26. G.R. Engelhardt and D.D. Macdonald, Monte-Carlo Simulation of Pitting Corrosion with a Deterministic Model for Repassivation, *J. Electrochem. Soc*., 2020, **167**, no. 1, 013540. doi: 10.1149/1945-7111/ab67a0
27. J.L. Li, C.T. Qu, S.D. Zhu, L. Liu and Z.Q. Gao, Pitting corrosion of super martensitic stainless steel 00Cr13Ni5Mo2, *Anti-Corros. Methods Mater*., 2014, **61**, no. 6, 387–394. doi: 10.1108/ACMM-08-2013-1293
28. N.U. Obeyesekere, 9 – Pitting corrosion, *Trends in Oil and Gas Corrosion Research and Technologies*, Elsevier Ltd, 2017, 215–248. doi:10.1016/B978-0-08-101105-8.00009-7

◆ ◆ ◆